ACS APPLIED MATERIALS & INTERFACES

Research Article

www.acsami.org

Enhanced Red Upconversion Emission, Magnetoluminescent Behavior, and Bioimaging Application of $NaSc_{0.75}Er_{0.02}Yb_{0.18}Gd_{0.05}F_4$@AuNPs Nanoparticles

Monika Rai,[†] Sunil Kumar Singh,*[,‡] Akhilesh Kumar Singh,[§] Ritika Prasad,[⊥] Biplob Koch,[⊥] Kavita Mishra,[†] and Shyam Bahadur Rai[†]

[†]Department of Physics, Banaras Hindu University, Varanasi-221005, Uttar Pradesh, India

[‡]Department of Physics, Indian Institute of Technology (BHU), Varanasi-221005, Uttar Pradesh, India

[§]Instituto de Ciencias Físicas, Universidad Nacional Autonoma de Mexico, Cuernavaca, Morelos, 62210, México

[⊥]Department of Zoology, Banaras Hindu University, Varanasi-221005, Uttar Pradesh, India

Supporting Information

ABSTRACT: The present study reports significant enhancement in the red upconversion emission of Er^{3+} in $NaSc_{0.8}Er_{0.02}Yb_{0.18}F_4$ upconversion nanoparticles (UCNPs), via a two step process, (i) codoping of Gd^{3+} ion at Sc^{3+} site and (ii) attaching gold nanoparticles (AuNPs) at the surface of these codoped nanostructures, and further probes the use of these Gd:UCNPs@AuNPs for bioimaging application. The Gd^{3+} codoping tailors the particle size (reduces) of UCNPs and bring out Er^{3+}−Yb^{3+} ion pair in close proximity, which promotes the cross relaxation mechanism and boosts the population in red emitting level $^4F_{9/2}$. Further, attachment of AuNPs on the surface of UCNPs gives 2-fold advantages, that is, reduction in green band (through resonance energy transfer with efficiency 31.54%) and enhancement in red band (through plasmonic effect). It gives red to green (R/G) ratio nearly 20:1 (almost single band red UC), which is quite promising for imaging application. In addition to this, codoping of Gd^{3+} enhances the magnetic moment appreciably and the obtained magnetic moment for $NaSc_{0.75}Er_{0.02}Yb_{0.18}Gd_{0.05}F_4$ UCNPs (~1.7 emu/g) is close to the reported values for bioseparation in case of NPs. This shows the potential of the material for multimodal (optical and magnetic both) imaging application. These magnetoluminescence particles were found safe up to 1 mg/mL dose as assessed by cytotoxicity measurement in human cervical cancer (HeLa) and lung cancer (A549) cells. Ultrafine nanoparticles, transparent, and stable colloidal solution and the unique red UC emission endow these NPs as optical probe for imaging applications.

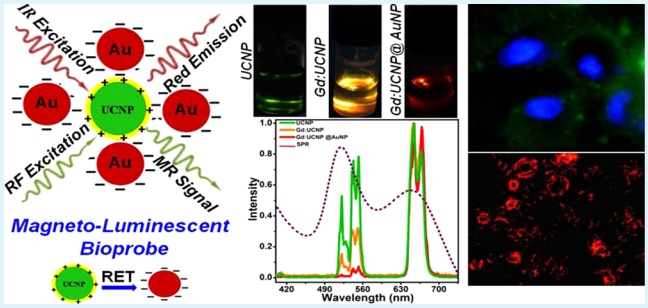

KEYWORDS: *lanthanide, nanoparticles, upconversion, paramagnetism, optical imaging*

1. INTRODUCTION

A long array of nanomaterials have been under active investigation for ultrasensitive fluorescent bioprobes. Among these, upconversion nanoparticles (UCNPs) are an excellent class of material for imaging applications with various photochemical advantages like thermal and optical stability, sharp emission bands, weak autofluorescence, lower toxicity, resistance to photobleaching, deep light penetration depth, long luminescence lifetime, multifunctionality, etc., over the conventional dyes or semiconductor quantum dots (QDs).[1−10] In past decade, Er^{3+}/Yb^{3+}-codoped $NaYF_4$ is recognized as one of the most efficient UCNPs, most intense peak lying in green region (520−550 nm), with the highest quantum yield reported until date.[11] Because of their excellent UC properties, this activator host combination have been identified suitable for many potential applications.

However, when it comes to use this host as bioprobe, it no longer remains the best choice. Because, the prominent green emission of Er^{3+} in this host is undesirable for imaging application, as the green emission may unnecessary produce background radiation, causing lowering of the signal-to-noise ratio (SNR). In principle, probe detection is governed mainly by emission intensity of the luminescent probe, optical path length through tissue and volumetric energy distribution. These properties significantly rely on to absorption and scattering properties of biological media and tissues. Red−NIR radiation (excitation/emission) is not (or negligibly) absorbed by biological samples, increases penetration depth in tissues, and avoids problems of light scattering background, etc., and so are most preferred for imaging applications.[12] These limitations have encouraged researchers to investigate other fluoride matrices, for example, LaF_3, $NaGdF_4$, $NaLuF_4$, KY_3F_{10}, CaF_2,

Received: April 14, 2015
Accepted: June 29, 2015
Published: June 29, 2015

DOI: 10.1021/acsami.5b03218
ACS Appl. Mater. Interfaces 2015, 7, 15339−15350

$NaLuF_4$, $BaLuF_5$, $KGdF_4$, $NaScF_4$, etc., for the suitable emission in red−NIR region.[13−16]

Among these, Er^{3+}/Yb^{3+}-codoped $NaScF_4$ shows efficient red UC emission suitable for imaging application.[17] The main theory behind the prominent red emission of Er^{3+} in this host is the exchange mechanism, which governs the rate of energy transfer involved between doped activator (Er^{3+} and Yb^{3+}) ions. According to this mechanism, there exist a short-range exchange interaction between nearest neighbor metal ions (here Sc^{3+}) and bridging ligand (here F^-), which is highly affected by effective ionic radius of the metal ions and the relative distance between them.[18,19] Since, Sc^{3+} (0.83 Å) possess smaller ionic radius, as compared to other lanthanide ion, for example, Y^{3+} (1.159 Å) and Gd^{3+} (1.193 Å), etc.; therefore, distance between Sc^{3+}−Sc^{3+} ions is also lower. This brings Er^{3+}−Yb^{3+} ion pair closer, when substituted at Sc^{3+} site, in $NaScF_4$ host compared to other hosts listed above. This fastens the rate of energy transfer between the ion pair (Er^{3+}−Yb^{3+}) and significantly enhances the cross relaxation which boosts the population in red emitting level $^4F_{9/2}$. In addition, this host crystallizes into two different types of crystals namely monoclinic Na_3ScF_6 to hexagonal $NaScF_4$, which also plays important role in color tuning.[17]

However, a long way still needs to follow to get almost single red UC band, which is the first aim of this study to deal with. Second, the multimodality of luminescent bioprobes has always attracted scientific community, especially for magnetic resonance imaging (MRI) and optical imaging together. Therefore, in the next step, idea is to introduce paramagnetic behavior in the sample in addition. In effect, Sc^{3+} itself shows paramagnetic behavior (having one unpaired electron in 3d shell), but very weak for imaging applications.[20] For the magnetic mode, Gd^{3+} ion has been an ever best choice (having seven unpaired electron in 4f shell) as contrast agents in MRI scans.[21,22] So, the idea is to codope Gd^{3+} ions, in addition, to bring out desired paramagnetic property. It has been reported that, effective magnetic moment of Sc matrix is enhanced in the presence of Gd^{3+} ion.[23] Also, incorporation of Gd^{3+} in certain matrix influences the growth mechanism, for example, induces the formation of smaller size particles and lowers the reaction temperature as well.[24,25] The smaller size particles may further favor cross relaxation (CR) and hence could help to enhance the red emission of Er^{3+} also.

To further induce single band UC emission in red region, resonance energy transfer (RET) from UCNPs to gold nanoparticles (AuNPs) has been used. There are numerous reports on the RET of UCNPs with various coupled systems like organic dyes, QDs, metal NPs, etc., or back energy transfer from Er^{3+} to Yb^{3+} to alter the UC emission.[26,27] Some reports also suggest the addition of transition metal ion like Mn^{2+} or Cr^{3+}.[28,29] However, these are site selective ions and therefore require a clever control on doping site. Of these, the metal NPs are incredibly comprehensive, easily synthesized, and undisruptive. The surface plasmon resonance (SPR) band in these metal NPs creates a local field effect, which enhances the excitation field as well as the emitted fluorescence which must be resonant with the SPR band. But, such plasmonic modulation property of metal NPs also leads to optical quenching or non radiative relaxation in some cases.[30,31] Since the SPR of AuNPs is known to appear near 520 nm, it is more suitable to alter the green emission in Er^{3+}/Yb^{3+} systems. Because of this resonance in energy, there are two possibilities: (i) the resonant oscillation of Au plasmons leading to enhancement in the overall UC intensity and (ii) energy transfer from Er^{3+}/Yb^{3+}:$NaScF_4$ to AuNPs leading to a decrease in green UC of Er^{3+} ion. Such phenomena require a strong coupling of the two systems (donors and acceptors) and hence strongly depend on the synthesis route.

In the present work, materials have been synthesized using thermal decomposition of metal compounds.[11] In the next step, a hybrid system of UCNPs with Au nanocolloid is prepared by using different surface functionalization strategies. The structural characterization including elemental analysis is carried out to confirm the phase, morphology and purity of UCNPs. A detailed steady state luminescence (UC) and decay time measurements have been carried out to explore the optical properties and energy transfer process. Magnetic characterization has been done to investigate the paramagnetic property of the UCNPs before and after Gd^{3+} doping. Cytotoxicity and UC-based microscopy have also been performed to test the utility of the material for optical imaging applications.

2. EXPERIMENTAL SECTION

2.1. Materials. All chemicals were of analytical grade and used without any further purification. Er_2O_3, Yb_2O_3, Gd_2O_3, $HAuCl_4{\cdot}3H_2O$ (purity 99.99% each), and oleic acid (OA) were purchased from Alfa Aesar; Sc_2O_3 (99.99%) from Himedia; NaOH (98%) and tri-sodium citrate (99%) were purchased from Fisher Scientific; NH_4F (95%), absolute ethanol, methanol, acetone, cyclohexane, 1-octadecene (ODE), and diethyl ether were purchased from Molychem; and L-lysine monohydrochloride (99%) was purchased from S. D. Fine-Chem Ltd. Nitrogen gas was used during the synthesis to create inert atmosphere.

For biological experiments, Dulbecco's modified eagle medium (DMEM) was purchased from Cellclone (Genetix Biotech Asia Pvt. Ltd.); fetal bovine serum (FBS), antibiotic solution (penicillin 1000 IU and streptomycin 10 mg/mL), and MTT (3-(4,5-dimethylthiazol-2-yl)-2,5 diphenyltetrazolium bromide dye) were purchased from Himedia, India, whereas DMSO (dimethyl sulfoxide) were obtained from Merck, India, and Hoechst 33342 was purchased from Sigma, USA.

2.2. Synthesis. *2.2.1. Synthesis of UCNPs.* In a typical process to prepare $NaSc_{0.8}Er_{0.02}Yb_{0.18}F_4$ (UCNPs), all rare-earth chlorides, in stoichiometric ratio, were mixed with 15 mL of OA in a three neck flask and heated at 150 °C for 30 min under constant stirring. Further, 40 mL of ODE is added to this mixture; the mixture is again heated at the same temperature for next 30 min, to form rare-earth oleate complexes, and then it was allowed to cool to room temperature. A solution (20 mL) of stoichiometric amount of NaOH and NH_4F in methanol is prepared separately and added to the first mixture slowly. A thick suspension is observed as a result which indicates for nuclei formation. This thick solution is then heated at 80 °C, with continued stirring, to evaporate methanol and complete consumption of fluorides far about 1 h. Further, the solution is subjected to reflux at 250 °C under N_2 flow for 1.5 h. This reflux gives rise to particle growth and Ostwald ripening. Solution is cooled to room temperature, precipitated by addition of absolute ethanol and extracted via centrifugation. The process is repeated for 4−5 times to wash the extra OA, and then dried overnight at 70 °C in a vacuum oven. A fine powder of UCNPs, easily dispersible in nonpolar solvents like cyclohexane, is obtained. The same protocol is followed to prepare $NaSc_{0.75}Er_{0.02}Yb_{0.18}Gd_{0.05}F_4$ (Gd:UCNPs) also.

2.2.2. Synthesis of L-Lysine Functionalized UCNPs. Further, to surface functionalize the UCNPs by L-lysine, first, it was essential to remove the oleate capping from the UCNPs. This was achieved by HCl treatment of 100 mg per 10 mL of aqueous solution of the oleate capped sample, pH of the solution is adjusted at 4 by addition of dilute HCl, followed by vigorous stirring for 4 to 6 h. This HCl treatment protonates the oleate ligand and the OA attached to the surface of UCNPs are rendered free, which is then extracted by addition of

DOI: 10.1021/acsami.5b03218
ACS Appl. Mater. Interfaces 2015, 7, 15339−15350

diethyl ether. The UCNPs were precipitated by acetone and collected via centrifugation.[32] The water dispersed solution of ligand free UCNPs is then mixed with lysine solution (100 μM) and stirred for 6 h at room temperature and then centrifuged to remove extra lysine. The lysine functionalized UCNPs thus obtained are washed with water and dried overnight in vacuum oven maintained at 70 °C.[33]

2.2.3. Synthesis of AuNPs and AuNPs Attached UCNPs. AuNPs were prepared by the reduction of gold hydrochlorate by trisodium citrate in aqueous solution.[34] For this reduction process, 2 mL of 1% trisodium citrate is added quickly in hot boiling 20 mL $HAuCl_4$ solution (1 mM) under constant stirring. The heating is removed only when the color of the solution turns deep red (in 5−10 min) indicating for the formation of monodisperse AuNPs. The surface of the citrate reduced AuNPs bears negative charge, while the lysine modification of the UCNPs yields positively charged UCNPs.[35] Therefore, when AuNPs are mixed in the dispersed solution of lysine modified Gd:UCNPs (2 mM), the AuNPs are efficiently attached on to the surface of Gd:UCNPs (Gd:UCNPs@AuNPs), obviously because of the Columbic interaction between the two oppositely charged entities. Figure 1 shows the pictorial representation of the complete process involved in this coupling mechanism.

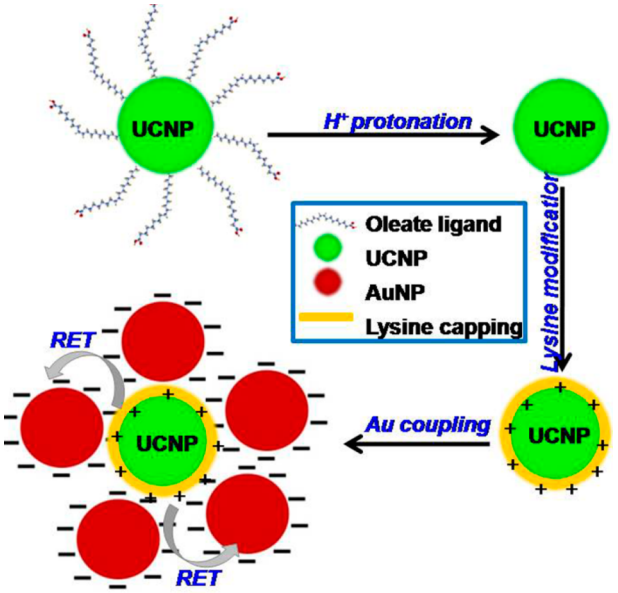

Figure 1. Coupling mechanism of gold nanoparticles (AuNPs) on the surface of upconversion nanoparticles (UCNPs).

2.2.4. Cytotoxicity Assay. The cytotoxicity of Gd:UCNPs@AuNPs on HeLa cells was accessed by MTT assay.[36] Briefly, 8000 (HeLa and A549) cells were seeded in a 96-well culture plate and left overnight for adherence in complete DMEM (DMEM, 10% FBS and antibiotic solution). The nanoparticle complex was prepared as stock solutions (5 mg/mL) from dry powder using sterile distilled water and then all working stock solution was prepared in culture media using the stock solutions as needed. Briefly, the stock solution was sonicated in a water bath sonicator immediately before diluting the solutions into complete DMEM. The cells were then exposed with the complex at various concentrations for 24 h at 37 °C in the presence of 5% CO_2. The cells were washed and 10 μL MTT (5 mg/mL) was added to each wells and it was incubated in dark for 2 h for the formation of formazan crystals. Further, to avoid interference of the nanoparticles we have employed the method described by Xia et al.[37] The plate was then read at 570 nm in a micro plate reader. The inhibitory concentration (IC_{50}) was measured from the absorbance ratio of the treated cells and control. The result was plotted as percentage (%) cell inhibition to that of the control cells using the formula,

$$\% \text{ inhibition} = (\text{control abs} - \text{sample abs})/(\text{control abs}) \times 100$$

2.2.5. Bioimaging. For UC imaging, HeLa cells (4×10^5 cells) were seeded in complete DMEM in a 6-well culture plate and allowed to adhere for 24 h at 37 °C in the presence of 5% CO_2. The cells were incubated in culture medium containing 800 μg/mL of Gd:UCNPs@AuNPs nanoparticles at 37 °C for 2 h. For fluorescence imaging, just before completion of incubation, an additional step of counterstaining with Hoechst 33342 (10 μg/mL; nuclear staining) was done for 20 min at 37 °C followed by washing of cells with PBS.[38,39]

2.3. Instrumentation. X-ray diffraction (XRD) patterns were recorded on a Bruker D8 advance powder diffractometer equipped with a sealed tube of Cu K_α X-ray source. High resolution transmission electron microscope (TEM) images were obtained on a FEI, Tecnai G^2, S-Twin instrument operating at 200 kV. Particle size was also measured using dynamic light scattering (DLS) method (Zetasizer Nano ZS, Malvern Instrument Ltd., UK). The instrument contains a 4 mW He−Ne laser operating at a wavelength of 633 nm and incorporates noninvasive backscatter optics (NIBS). Vibrational measurements were carried out on Fourier transform infrared (FTIR) spectrometer (PerkinElmer, Frontier series) in attenuated total reflection (ATR) mode. Each spectrum was the average of 8 scans with a resolution (scan rate) of 2 cm^{-1}. UV−visible absorption measurement of Au nanocolloid is recorded on PerkinElmer, Lambda-750 spectrometer. The upconversion measurement was done using an iHR320 Jobin Yvon spectrometer equipped with R928 photo multiplier tube. The excitation source used was a diode laser (CW, 600 mW) lasing at 980 nm. The samples for UC measurements were prepared by dispersing 1 mg powder in 3 mL solvent followed by sonication for 5 min. For decay time measurement, the laser light was made pulsed using a mechanical chopper (400 Hz) and data were acquired using a monochromator, oscilloscope (analog digital scope-HM1507) and software (SP107). For the magnetic measurement, quantum design vibrating sample magnetometer (VSM) of physical property measurement system (PPMS, model No. 6000-14T) has been used. The VSM oscillation frequency was calibrated at 40 Hz with the typical oscillation amplitude of 1 mm peak. For cytotoxicity, the absorbance of the purple formazan solution was read under 570 nm radiation using a micro plate reader (Microscan (MS5608A), India). The Cat Scope (model CS-IB1000) inverted microscope equipped with camera Cat Cam (model Cat Cam 200) was used for UC imaging (using diode laser). For fluorescence imaging, EVOS FL (Life Technologies) cell imaging system (AMF4300) with GFP filter (Ex-470 nm and Em-510 nm) equipped with high sensitivity monochrome CCD camera was used.

3. RESULTS AND DISCUSSION

3.1. Structural Characterization. The typical XRD patterns of UCNPs and Gd:UCNPs are shown in Figure 2. The XRD peaks match well with the dominant hexagonal β-phase of $NaScF_4$ with lattice parameters $a = b = 12.97$ Å, $c =$

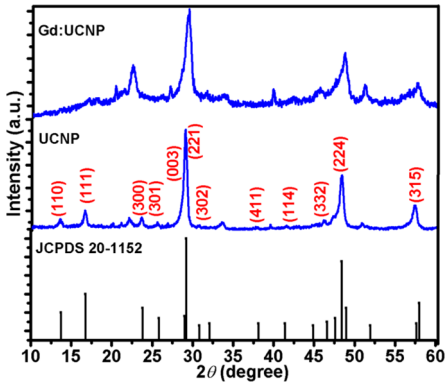

Figure 2. X-ray diffraction (XRD) patterns of $NaSc_{0.8}Er_{0.02}Yb_{0.18}F_4$ (UCNP) and $NaSc_{0.75}Er_{0.02}Yb_{0.18}Gd_{0.05}F_4$ (Gd:UCNP).

DOI: 10.1021/acsami.5b03218
ACS Appl. Mater. Interfaces 2015, 7, 15339−15350

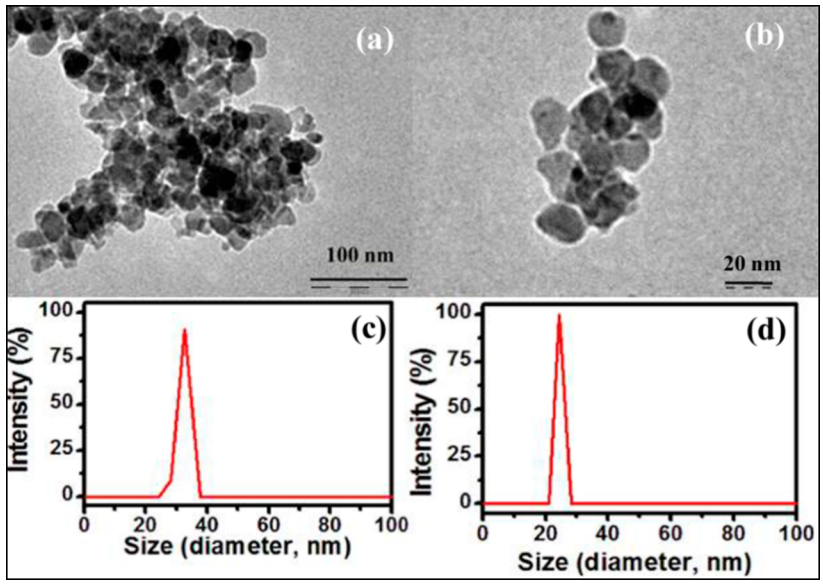

Figure 3. Transmission electron microscopy (TEM) images and dynamic light scattering (DLS) measurements: (a, c) $NaSc_{0.8}Er_{0.02}Yb_{0.18}F_4$ and (b, d) $NaSc_{0.75}Er_{0.02}Yb_{0.18}Gd_{0.05}F_4$ nanoparticles, respectively.

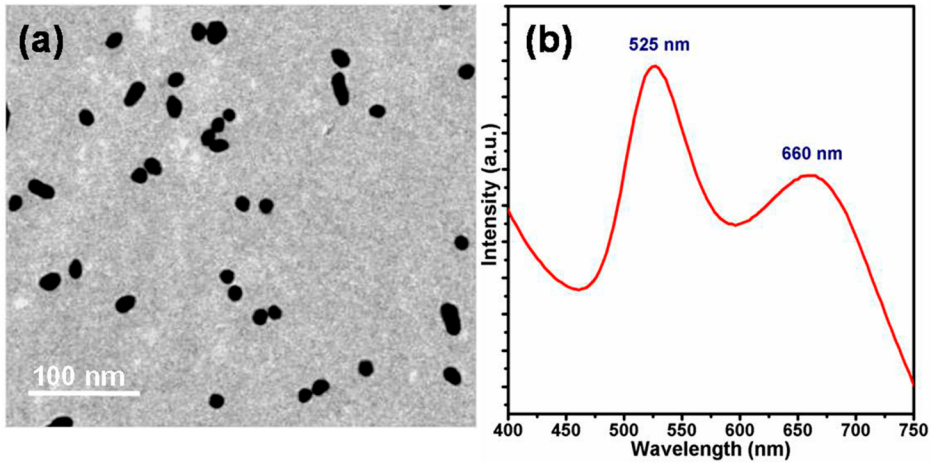

Figure 4. (a) Transmission electron microscopy (TEM) image of AuNPs and (b) UV−visible absorption spectrum of Au nanocolloid.

9.27 Å and $\alpha = \beta = 90°$, $\gamma = 120°$, corresponding to the JCPDS file No. 20-1152.

The ratio of polar surfactant oleic acid to the non polar solvent octadecene is 3:8, which is nearly an optimum polar medium for the evolution of hexagonal phase.[17] However, a few weak diffraction peaks corresponding to the monoclinic phase of Na_3ScF_6 (JCPDS 20-1153) also appears. There is no signature of dopant ions (Er, Yb, and Gd), which confirms the effective doping at Sc^{3+} site. The Gd:UCNPs also show the formation of the dominant hexagonal phase. Here, however, the XRD peaks are broadened which suggests for the formation of fine particles with much smaller size than that of UCNPs.

Figure 3a and b show TEM images of UCNPs and Gd:UCNPs. It is obvious from images that Gd^{3+} codoping tailors (reduces) the particle size from 32 (±7) nm (for UCNPs) to 25 ± 5 nm (Gd:UCNPs). The similar results are also confirmed through DLS measurements; corresponding DLS results are shown in Figure 3c and d. It has already been established by Wang et al. through density functional theory (DFT) calculations that, the substitution of an ion of larger radius (here Gd^{3+}) at the place of another ion of smaller radius (e.g., Sc^{3+}) enhances the electron charge density on the crystal surface.[25] This enhancement in the electron charge density on the surface reduces the rate of diffusion of F^- ions on to the surface of the crystal and hence formation of nuclei is limited profoundly. Thus, the particle size tuning after Gd^{3+} codoping in the matrix is mainly due to limited nuclei formation which in turn limits the particle growth. Now, the particle size is in the range of 20−30 nm which is narrow enough for bioimaging applications. There is no appreciable change in the morphology of Gd:UCNPs. The compositional analysis of the UCNPs has also been performed through the energy dispersive X-ray (EDX) spectrum; see the Supporting Information Figure S1. This analysis confirms the presence of Na, Sc, F, Yb and Er in the sample; and the atomic ratio of constituents Na/Sc/F/Yb/Er is found as 0.92/0.87/4.97/0.28/0.02, which is pretty close to the stoichiometric ratio, that is, 1/0.8/4/0.18/0.02. This confirms the formation of desired NPs.

Further, since gold nanocolloids have also been used to tune the color of the UC emission; therefore, it becomes essential to characterize the structure and optical behavior of the synthesized AuNPs also. Figure 4a shows the TEM image of

DOI: 10.1021/acsami.5b03218
ACS Appl. Mater. Interfaces 2015, 7, 15339−15350

as-synthesized AuNPs, while Figure 4b shows the UV−visible absorption spectrum of the diluted AuNPs in water medium. It is obvious from the TEM image that the synthesized particle are monodisperse and spherical in nature. Some particles are elongated too and deviate from spherical morphology. The average particle size is ∼14 nm. The prominent surface plasmon resonance (SPR) absorption bands due to these AuNPs are observed at 525 nm, corresponding to transverse SPR of Au nanospheres, and at 660 nm, corresponding to longitudinal SPR of Au nanorods.[40] It is well-known that citrate reduced gold chloride yields both the structures and they are further stabilized with CTAB etc. to get homogeneous morphology, if required. However, in the present work, no stabilizing agent is used and so both the SPR bands are present in the UV−visible absorption spectrum.

In an attempt to prepare the hybrid system of Gd:UCNPs@AuNP, it becomes essential to monitor the morphology of this hybrid to observe the degree of intactness. Figure 5 shows the

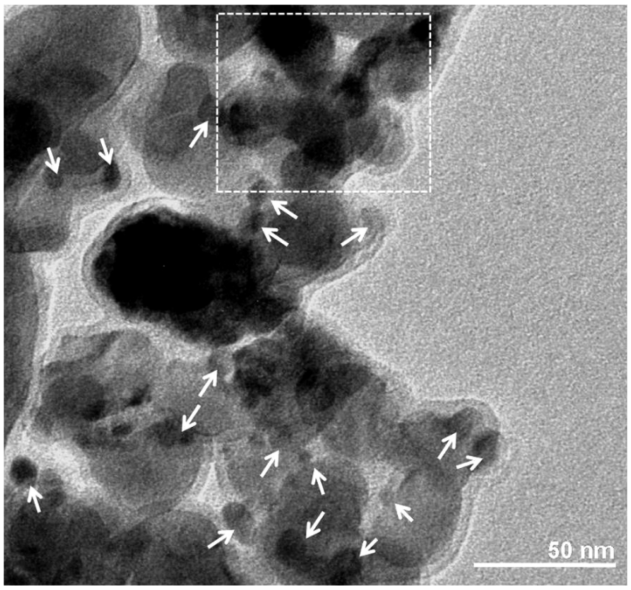

Figure 5. Transmission electron microscopy (TEM) image of Gd:UCNPs@AuNP. White arrows mark the attachment of AuNPs over Gd:UCNP.

TEM image of Gd:UCNPs@AuNPs system and clearly reveals the attachment of AuNPs over UCNPs. The Lysine capping of UCNP over which AuNPs are stuck can also be seen in the image clearly. The white arrows clearly mark the attachment of AuNPs. As far as size of the hybrid is concerned, it is the combined value of UCNPs and AuNPs as shown in the particle size distribution graph in Supporting Information Figure S4. The particle under the white square marked in the TEM image supports this fact and is also in accordance with our pictorial model as shown in Figure 1. There is an increment in the particle size of the UCNPs@AuNPs, from 20 to 30 nm (for UCNPs) to ∼35 nm, which is obvious due to gold attachment. Some particles seem to as big as 50−60 nm, though, their numbers are very less. However, the case is not uniform throughout the image and there is random number of AuNPs bound to the UCNPs. Therefore, the enhancement in size of the hybrid NPs is not isotropic.

In the next step, FTIR studies have been carried out to probe the different types of surface functionalization of UCNPs. Figure 6 shows the FTIR spectra of UCNPs with oleate capping, bare UCNPs and lysine capped UCNPs. The oleate

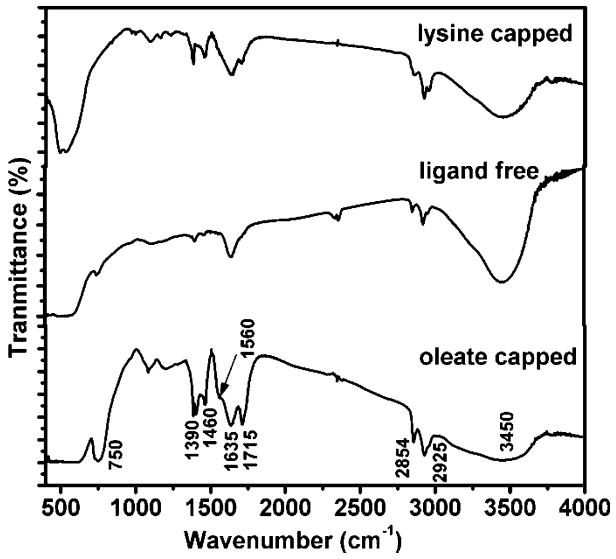

Figure 6. Fourier transform infrared (FTIR) spectra of oleate capped, bare and lysine capped $NaSc_{0.75}Er_{0.02}Yb_{0.18}Gd_{0.05}F_4$ nanoparticles.

capped UCNPs show the presence of characteristic peaks of oleic acid at 750 cm^{-1}. The other two pairs of strong peaks at (2854, 2925) cm^{-1} and (1460, 1560) cm^{-1} are attributed to the asymmetric and symmetric stretching vibrations of methylene group ($-CH_2-$) and carboxyl group ($-COO^-$) groups in oleic acid, respectively.

The band at 1715 cm^{-1} arises due to the C═O stretching vibration of oleic acid. A broad peak at 3450 cm^{-1} corresponds to the stretching vibration of hydroxyl group (υ_{OH}) while the peak near 1635 cm^{-1} is due to the bending modes of hydroxyl group (δ_{OH}). A broad peak due to stretching vibration of NO (υ_{NO}) appears around 1390 cm^{-1}.[32] Surface adsorbed NO^{3-} group is responsible for this quenching entity. After removal of ligands by solvent extraction of diethyl ether, the peaks of different stretching vibration corresponding to oleate group are significantly reduced indicating that the oleate ligand was removed from the surface of UCNPs. Further, upon lysine capping, the peaks corresponding to the stretching vibrations of carboxyl group again reappears with additional bands at 2924 and 2960 cm^{-1}, signature peaks due to amine group. This lysine capped UCNPs are evenly dispersed in aqueous medium.

3.2. Steady State Optical Measurement Analysis.

3.2.1. Frequency UC Studies of $NaSc_{0.8}Er_{0.02}Yb_{0.18}F_4$ NPs (UCNPs). Figure 7a shows a typical room temperature frequency UC spectrum of UCNPs under the 980 nm excitation. The concentration of 2 mol % Er and 18 mol % Yb has already been verified optimal for the maximum emission intensity in rare-earth fluoride hosts.[25] The same result is obtained in the present study also and the inset to Figure 7a shows a variation in emission intensity with Er^{3+} concentration, keeping Yb^{3+} concentration fixed, with maximum at 2 mol %. The spectrum exhibits an intense green band centered at 553 nm due to $^2H_{11/2}$ ($^4S_{3/2}$) → $^4I_{15/2}$ transition; an intense red band at 653 nm due to $^4F_{9/2}$ → $^4I_{15/2}$ transition; and relatively weak emission bands in blue and IR regions attributed to $^2H_{9/2}$ → $^4I_{15/2}$ and $^2I_{9/2}$ → $^4I_{15/2}$ transitions, respectively. The overall UC mechanism is explained through the partial energy level

DOI: 10.1021/acsami.5b03218
ACS Appl. Mater. Interfaces 2015, 7, 15339−15350

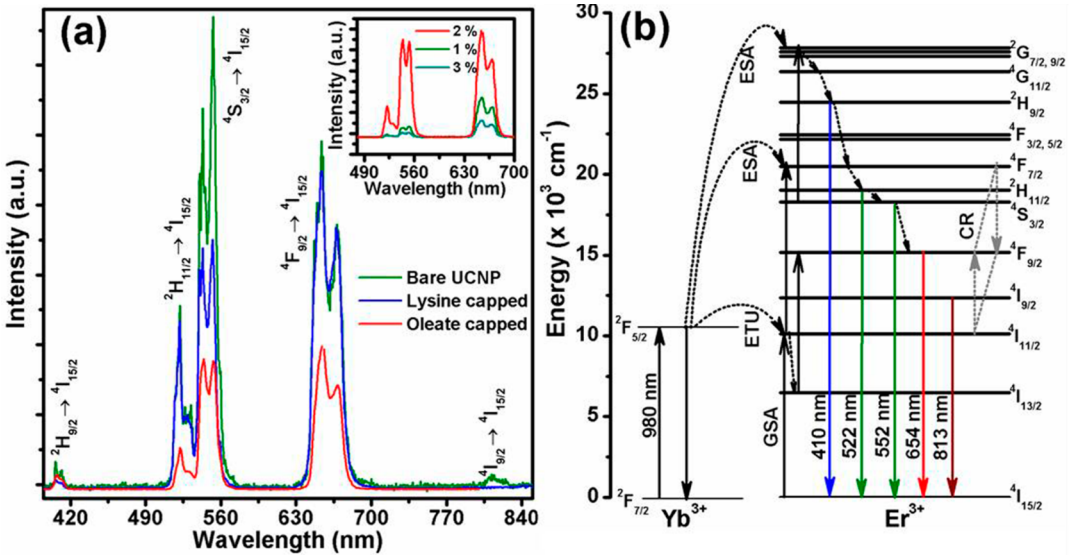

Figure 7. (a) Upconversion emission spectra of $NaSc_{0.8}Er_{0.02}Yb_{0.18}F_4$ nanoparticles with and without ligand. Inset shows a variation in UC emission intensity with a variation in Er^{3+} concentration, and (b) shows the partial energy level scheme of Er^{3+} and Yb^{3+} ions showing different mechanism of upconversion.

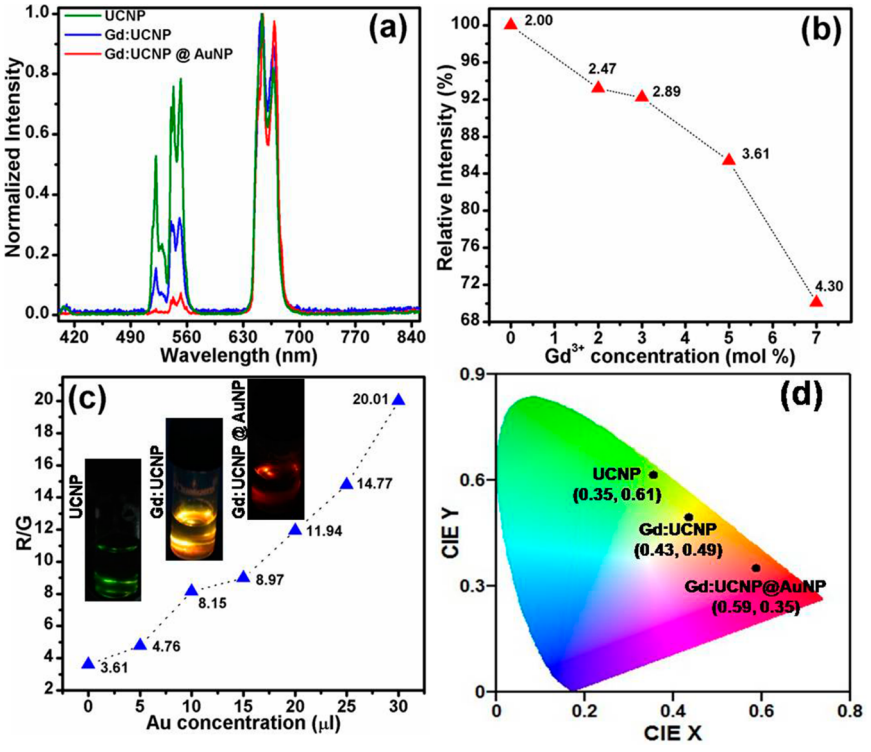

Figure 8. (a) Effect of Gd^{3+} codoping and attachment of AuNPs on the UC emission of UCNPs. (b) Change in the overall UC emission intensity (given in %) with a variation in the concentration of Gd^{3+} ions. Numerical values are R/G ratios. (c) Variation of R/G ratio with varying concentration of AuNPs in Gd:UCNPs. Inset shows the digital pictures of color of UC emission showing color tuning from green to yellow to deep-red. (d) CIE diagram with position of color coordinates.

diagram of Er^{3+} and Yb^{3+} ions, shown in Figure 7b. In the first step, a pump photon at 980 nm (10 245 cm^{-1}) excites Yb^{3+} ions to $^2F_{5/2}$ level which resonantly transfers its energy to nearby Er^{3+} ions (energy transfer upconversion, ETU) and thus promotes Er^{3+} ions from ground state to $^4I_{11/2}$ state. From here, most of the population relaxes to $^4I_{13/2}$ level through non radiative relaxation. The population in $^4I_{11/2}$ and $^4I_{13/2}$ levels absorb a second incident photon and get promoted to $^4F_{7/2}$ and $^4F_{9/2}$ levels, respectively (excited state absorption, ESA). Population from $^2H_{11/2}/^4S_{3/2}$ and $^4F_{9/2}$ levels relax to the ground state $^4I_{15/2}$ radiatively resulting in efficient green and red emission. Third photon absorption from the metastable state $^4S_{3/2}$ finally populates $^2H_{9/2}$ level responsible for a blue emission. Similarly $^4I_{9/2}$ level also gets populated through various nonradiative channels from upper excited state and gives IR emission. Thus, the intense red and green emission is due to two photons and blue emission is through the involvement of three photons.

DOI: 10.1021/acsami.5b03218
ACS Appl. Mater. Interfaces 2015, 7, 15339−15350

The effect of surface ligand is clearly observed in terms of the relative intensities of red and green emission which largely depends on the rate of non radiative channels i.e. multiphonon relaxations (MR). The MR rate (K_p) is given by[41]

$$K_p = A \exp^{-Bp} \text{ and } p \approx \Delta E/\hbar\omega \quad (1)$$

Here, A and B are host constants, p is the number of phonons involved, ΔE is the difference between two energy levels, and $\hbar\omega$ is the maximum energy of single phonon. Usually, for $p \leq 5$ the non radiative MR process dominates over radiative process. In the present case, due to abundant organic groups like OH, $-CH_2$, $-CH_3$, C═O, etc., the phonon energy is strongly enhanced. This facilitates an easy MR between $^4I_{11/2}$ and $^4I_{13/2}$ levels. Population in $^4I_{13/2}$ level further goes to $^4F_{9/2}$ through ESA process which is the direct consequence of intense red emission.[42] Also, the direct population of $^4F_{9/2}$ level through $^4S_{3/2}$ or $^2H_{11/2}$ state is also facilitated, which can effectively enhance red emission and decrease the green emission at the same time. Hence, we get prominent red emission in oleate capped NPs.

One additional factor contributing to the population of $^4F_{9/2}$ and dominant red emission is the cross relaxation (CR) mechanism owing to the large number density of the dopant ions (Er^{3+}, Yb^{3+}) and the shorter distance between Er^{3+}−Yb^{3+} ion pair. Because of the large concentration, the relative distance between the nearby Er^{3+} ions are reduced and a part of radiative energy is easily relaxed or exchanged with the neighbor ion (as discussed in the Introduction section) which in turn populates $^4F_{9/2}$ level.[38] This mechanism is shown in Figure 7b in the energy level diagram by a close loop and represented as $(^4F_{7/2} \rightarrow {}^4F_{9/2}) \leftrightarrow (^4I_{11/2} \rightarrow {}^4F_{9/2})$. However, after removing the oleate capping from the surface of NPs, there is significant enhancement the UC intensity, nearly five times enhancement is observed. Similarly, when we surface functionalize UCNPs using lysine the UC emission intensity again get reduced obviously due to MR introduced due to organic quenching centers.

3.2.2. Tuning Red to Green (R/G) Ratio of the UC Emission: Effect of Gd^{3+} and AuNPs. Figure 8a shows the effect of Gd^{3+} codoping (also the effect of AuNPs given in next section) on the UC emission of UCNPs. The normalized spectrum shows a clear picture of a change in R/G ratio for 0 and 5 mol % Gd^{3+} codoped samples. There are two main reasons behind this rapid change in R/G ratio. First one is the ionic radius of Gd^{3+} which is the largest among all the other dopant ions (Er^{3+} and Yb^{3+}) replacing the Sc^{3+} (relatively much smaller ionic radius) ions in $NaScF_4$ matrix. This mismatch in ionic radius causes strain in the crystal lattice and brings out the Er^{3+}-Yb^{3+} ion pair closer. The close proximity between Er^{3+}−Yb^{3+} ions promotes the CR mechanism and thus enhances the red UC emission and thereby R/G ratio is also enhanced. The second region is obviously due the formation of smaller nanocrystals in the presence of Gd^{3+} ions. The reduction in particle size increases surface to volume ratio and so the surface of the NPs become more active and attracts various surface defects, which put off the frequency UC and the intensity of green emission is diminished considerably. However, this process does not promote the red emission in any way, actually; as a consequence overall emission is diminished. Figure 8b shows a change in the overall emission intensity (given in %) with a variation in the concentration of Gd^{3+} ions in $NaSc_{0.80}Er_{0.02}Yb_{0.18}F_4$ NPs. It is clear from the graph that up to 5 mol % concentration of Gd^{3+} ion the reduction in intensity is only 10% (which is considerable) but beyond 5 mol % concentration of Gd^{3+} ion the intensity decreases stridently and so further studies in the presence of AuNPs have been considered with 5 mol % concentration of Gd^{3+} ion.

UV−visible absorption spectrum of the AuNPs clearly shows two prominent surface plasmon resonance (SPR) bands at around 525 and 660 nm, which overlap strongly with the green and red UC emission bands of Er^{3+} ion in $NaScF_4$ matrix. Thus, in principle, there arises two possibilities: one is the plasmon induced intensity enhancement (plasmonic effect), and the other is the resonance energy transfer from UCNPs to AuNPs. The RET can be easily observed to take place in the present sample based on the fact that (i) there is a good spectral overlap between the donor emission (Gd:UCNPs) and acceptor absorption (AuNPs) (D−A) pair and (ii) Columbic interaction prevails owing to the oppositely charged D (positive)−A (negative) species. As stated, a significant reduction in green UC emission band of Er^{3+} is observed after the addition of AuNPs in Gd:UCNPs.

Figure 8c shows a variation of R/G ratio with varying concentration of AuNPs in Gd:UCNPs. It is easily inferred from the graph that, R/G ratio consistently increases with increasing concentration of AuNPs. However, the overall intensity also decreases as well, simply because the high concentration of AuNPs surrounds large number of Gd:UCNPs and therefore excitation becomes poor. Therefore, 30 μL of AuNPs have been used as maximum and it gives R/G ratio nearly 20:1. This value of R/G is quite promising (almost single band red emission) and best reported so far, exceeds the previously reported value 13:1.[29] Figure 8d shows the chromaticity (CIE) diagram with position of color coordinates for the three different samples. It is apparent that the emission shifts from green to yellow in case of Gd:UCNPs and subsequently to red emission for Gd:UCNPs@AuNPs. Digital images of aqueous solution of UCNPs, Gd:UCNPs and Gd:UCNPs@AuNPs gives a clear visual perception of the result drawn through CIE diagram, see inset to Figure 8c.

Further, an anomalous behavior is noticed in the pattern of intensity variation of the green and red UC emission bands of Gd:UCNPs@AuNPs. The green emission is reduced which is obvious due to RET as stated earlier. However, at the same time, there is enhancement in the red UC emission intensity as well, see Supporting Information Figure S2. At the first moment, it is simple to consider this enhancement being due to plasmonic effect of SPR band at 660 nm. Though, if we look into the literature, there is no such report available which probes both the phenomena (energy transfer and plasmonic effect) to occur simultaneously, yet, the study by Volkov et al., which states that the rod like structure has more pronounced effect in plasmonic enhancement, supports our finding. As a result of this effect, longitudinal mode is more efficient in the amplification of fluorescence and is less damped as compared to the transverse SPR.[40] This is due to a simple phenomenon of electrostatics termed as "lighting of rods". According to this phenomenon, there is high surface charge density at the vertices which results in significant field enhancement and coupling of fields.[43] The surface plasmon resonance of particles on the surface of such systems acts to increase the local field at an adsorbed molecule and amplify the emitted radiation. Thus, apart from the plasmonic enhancement due to dipolar fields, which is related to the optical properties of the surface, there arises a geometrical factor also.

DOI: 10.1021/acsami.5b03218
ACS Appl. Mater. Interfaces 2015, 7, 15339−15350

The correlation of longitudinal and transverse mode is given by relation[44]

$$\lambda_L = (33.34R - 46.31)\varepsilon + 472.31 \quad (2)$$

where λ_L is maximum wavelength corresponding to longitudinal mode, R is the aspect ratio, and ε is the dielectric constant of the medium. For a constant ε, λ_L has a linear variation with R. For water medium, this relation gives $R \approx 1.45$, which is clearly observed for at least few AuNPs in Figure 4a. Since the deviation of R from 1 is not so high (1.45 only) and the number of nanorods are also less compared to nanospheres, consequently, the effect of SPR at 660 nm is weaker as compared to SPR at 525 nm, as is apparent in Figure 4. Thus, the enhancement in red emission (via plasmonic effect) is not so profound as compared to reduction in green emission (via RET process). However, the combined effect enhances the R/G ratio appreciably.

3.3. Time Domain Optical Measurement Analysis. Time domain studies have been further carried out to confirm RET from Gd:UCNPs to AuNPs. Figure 9 shows the decay

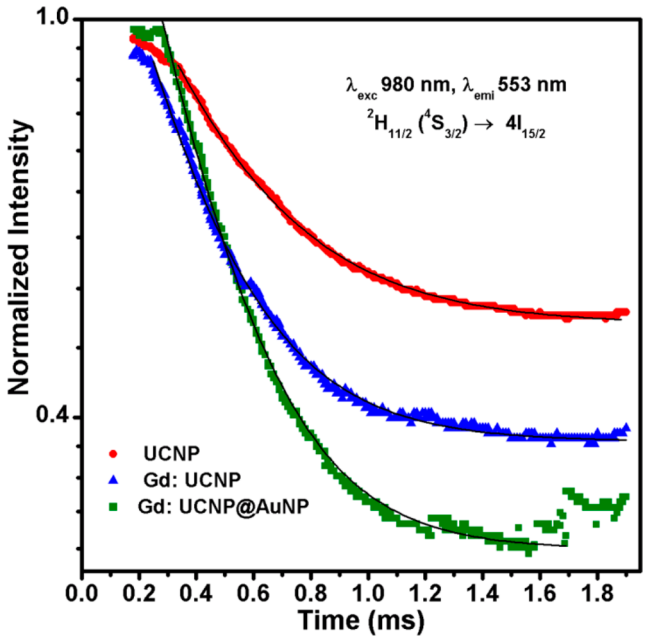

Figure 9. Decay curves for the green transition ($^4S_{3/2} \rightarrow {}^4I_{15/2}$) of Er^{3+} (λ_{ex}= 980 nm) in UCNPs, Gd:UCNPs, and Gd:UCNPs@AuNPs.

curves for the green level of Er^{3+} ($^4S_{3/2} \rightarrow {}^4I_{15/2}$) for UCNPs, Gd:UCNPs and Gd:UCNPs@AuNPs. The trend of lifetime values is 355.44, 273.75, and 245.59 μs, respectively. All the values have been determined by fitting the decay curves with monoexponential decay up to 3 places of decimal. This decrease in lifetime values is completely in accordance with the emission spectrum shown in Figure 8a. The decrease in lifetime after addition of AuNPs clearly support our explanation of resonance energy transfer from Gd:UCNPs to AuNPs. The energy transfer efficiency (ξ) has been calculated using the relation

$$\xi = 1 - \left(\frac{\tau_{D-A}}{\tau_D}\right) \quad (3)$$

where τ_{D-A} and τ_D is the lifetime of donor ion in presence and absence of acceptor, respectively. Thus, for AuNPs, as an acceptor, ξ is 31.54% which is appreciable and accounts a significant RET phenomena. Further, for the red emitting level ($^4F_{9/2} \rightarrow {}^4I_{15/2}$) of Er^{3+} ion, the trend of lifetime is reversed and it shows an ascending order if we compare the lifetime, that is, 364.02 μs for UCNPs, 377.73 μs for Gd:UCNPs, and 388.76 μs for Gd:UCNPs@AuNPs. Decay curves are shown in Supporting Information Figure S3.

However, the rate of change is slower as compared to the green level. The enhancement in lifetime after addition of AuNPs is the eye catching factor, which supports the fact that the SPR band at 660 nm enhances the red emission of Er^{3+}. This small increase in lifetime of red level is also expected due to CR which populates $^4F_{9/2}$ dominantly.

3.4. Magnetic Characterization. Figure 10 shows the room-temperature magnetization of UCNPs and Gd:UCNPs as

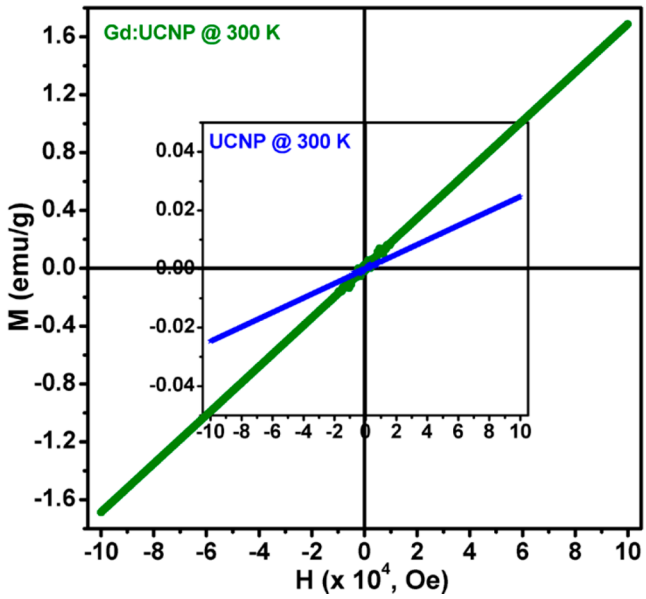

Figure 10. Room-temperature magnetization of UCNPs (central) and Gd:UCNPs as a function of applied field (H) up to 10 T.

a function of applied field (H) up to 10 T. Magnetic moment of $NaScF_4$ is completely unexplored and author first time observe that it shows a linear behavior, that is, paramagnetic nature. The magnetic moment observed for UCNPs is 0.02 emu/g, which is much weak for imaging application (MRI). However, codoping of Gd^{3+} enhances the magnetic moment appreciably and an enhancement of almost 2 orders of magnitude (more than 80 times) in magnetic moment is attained with 5 mol % of Gd^{3+} ions. The obtained magnetic moment for Gd:UCNPs is ~1.7 emu/g, which is pretty close to the reported values for bioseparation in case of NPs and thus is suitable for MRI applications.[45] The paramagnetic behavior of the Gd^{3+} ions originates from seven unpaired electrons in 4f shell, which are closely shielded by the outer shell ($5s^25p^6$) electrons from the crystal field, that is, the associated magnetic moments are all localized and noninteracting.[46] The $M-H$ curve shows some noise (random points) initially at low applied magnetic field. This is due to the presence of nanosize particles in the sample which show random motion and disturb the exact magnetic moment.

Paramagnetic behavior is further explored by measuring temperature dependent magnetization with ZFC (zero field cooling) protocol at 1 T (5–300 K), and FC (field cooling)

DOI: 10.1021/acsami.5b03218
ACS Appl. Mater. Interfaces 2015, 7, 15339–15350

protocol at 1 T (5−120 K), curves are shown in Figure 11a and b. The curves clearly depict that, the magnetic susceptibility

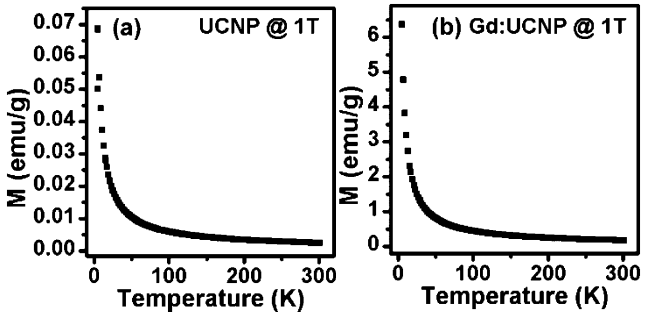

Figure 11. Temperature dependent magnetization with zero field cooling (ZFC) protocol at 1 T (5−300 K) and field cooling (FC) protocol at 1 T (5−120 K) for (a) UCNPs and (b) Gd:UCNPs.

increases with a decrease in temperature; a typical behavior of paramagnetic materials as explained by Curie−Weiss law, which suggest that there is no magnetic coupling between the spins at low temperature. Further, ZFC and FC curves completely overlap with each other which are a typical behavior of superparamagnetism. Thus, the finding shows promises of the material for its wide applications including MRI.[47]

3.5. Bioimaging. *3.5.1. Cytotoxicity.* The cell viability data obtained with the MTT assay in HeLa cells has been shown in Figure 12. The result shows that the Gd:UCNPs@AuNPs

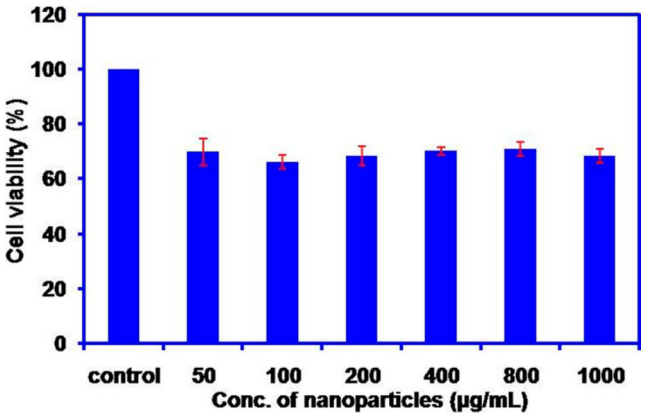

Figure 12. Cytotoxicity of Gd:UCNPs@AuNPs against HeLa cells after 24 h incubation at various concentrations (μg/mL). Data are expressed as a percentage of control ± SEM (standard error mean) from 3 replicates.

nanoparticle does not induce any cytotoxic effect on HeLa cells. The cell viability remained 70% even at a high concentration of 1 mg/mL, indicating positive biocompatibility of the complex. This result suggests that the nanoparticles can be used safely for bioimaging applications. The cytotoxicity of Gd:UCNPs@AuNPs (0−1 mg/mL, for 24 h, in HELF cells) has been reported by another group also. They also observed that the cell viability remained unaffected even at 1 mg/mL of ATF/AEP-coupled $NaScF_4$ NPs and shows cell viability well above 90%, making it safe for luminescent biolabeling.[38]

To supplement the above result, we also performed the cytotoxicity measurement in A549 cell line (lung cancer cell line) and the cell viability data obtained with A549 cells is shown in Figure 13. The result shows that the Gd:UCNP@

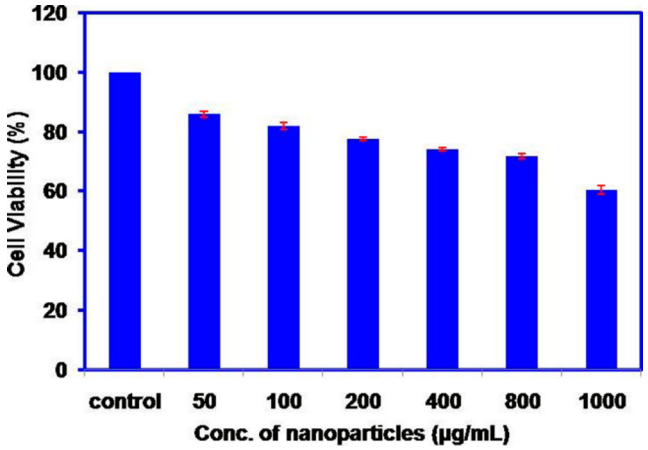

Figure 13. Cytotoxicity of Gd:UCNPs@AuNPs against A549 (lung cancer) cells after 24 h incubation at various concentrations (μg/mL). Data are expressed as a percentage of control ± SEM from 3 replicates (n = 3).

AuNPs does not induce cytotoxic effect on A549 cells also. At lowest concentration the cell viability was about 85% and the viability was found up to 60% even at highest concentration of 1 mg/mL. Thus, the result obtained with lung cancer cell (A549) seems to be similar to that of cervical cancer cells (HeLa) which confirms that the nanoparticles are safe for bioimaging applications up to the tried dosage.

3.5.2. Optical Imaging. The data obtained from MTT assay proves the suitability of this material for bioimaging application. So in the first step, inverted fluorescence microscopy images of HeLa cells, incubated with Gd:UCNPs@AuNPs nanoparticles at 800 μg/mL concentration, were observed. HeLa cells showed distinct green fluorescence (because of well-known photoluminescence of Er^{3+} under UV excitation) as shown in Figure 14 indicating uptake of Gd:UCNPs@AuNPS. Particles seem to accumulate mainly in the cell membrane along with some accumulation in the cytoplasmic region. However, the nuclear region is mostly excluded, which is traced on

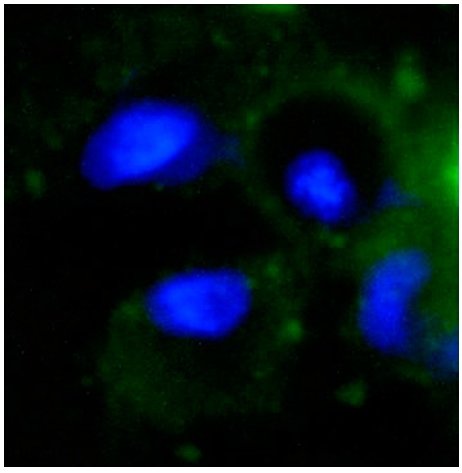

Figure 14. Fluorescence images of HeLa cells incubated with Gd:UCNPs@AuNPs (800 μg/mL) for 2 h at 37 °C. Hoechst 33342 counterstaining indicate nuclear region (blue) with accumulation of fluorescent (green) particle in the membrane and cytoplasmic region of the cell as observed under inverted fluorescence microscope (Evos, FL).

DOI: 10.1021/acsami.5b03218
ACS Appl. Mater. Interfaces 2015, 7, 15339−15350

counterstaining the cells with DNA binding Hoechst 33342 dye, which gives intense blue color via normal fluorescence. Further, after confirming the uptake of hybrid nanoparticles, UC-based imaging was performed. Figure 15 shows the UC

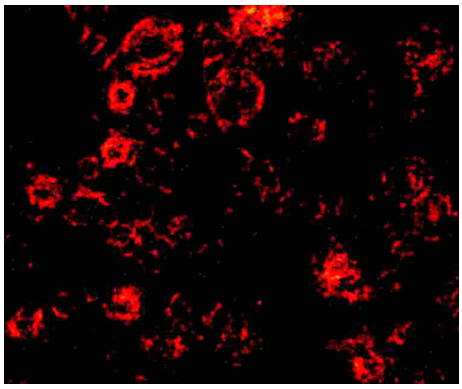

Figure 15. UC images of HeLa cells after incubation with Gd:UCNPs@AuNPs nanoparticles (800 μg/mL) for 2h at 37 °C.

images (dark field images) of HeLa cells visualized under inverted microscope at 980 nm excitation. The hybrid NPs accumulated in the cells gives beautiful visualization of red UC emission (in the particular field of area) where the IR beam is incident. A clear picture of the cell with uptake of the nanoparticles in the cells, along with accumulation mainly in the membrane region is observed in the UC imaging also.

The deep-red signal observed showed the existence of potential UC emission from the cells, and it makes obvious that the hybrid system is stable in the biological media/cells as well. Different studies involving UCNPs showed that they are useful for both fluorescence and dark field imaging.[48−50] Thus, the imaging through both the fluorescence as well as UC emission indicates that NPs are internalized by the cells and could be used in cellular imaging effectively.

4. CONCLUSION

Magnetoluminescent upconversion nanoparticles $NaSc_{0.75}Er_{0.02}Yb_{0.18}Gd_{0.05}F_4$@AuNPs have been synthesized and used for optical-imaging application. The codoping of Gd^{3+} ions and an efficient resonance energy transfer from Er^{3+} to AuNPs tailors UC emission of Er^{3+} such that red to green (R/G) ratio is 20:1, which is best reported so far. The material exhibits paramagnetic nature (magnetic moment ∼1.7 emu/g), which also makes it promising for multimodal imaging. These magnetoluminescence particles were found safe as assessed through cytotoxicity measurement over an incubation period of 24 h. The cell imaging data also promotes it as a suitable candidate for bio imaging, but further detailed studies regarding subcellular target or as a bioprobe is needed.

■ ASSOCIATED CONTENT

Supporting Information

Energy dispersive X-ray (EDX) spectrum of $NaSc_{0.8}Er_{0.02}Yb_{0.18}F_4$ nanoparticles, emission spectrum showing reduction in green band and enhancement in red band with addition of AuNPs, and decay curves for the red transition ($^4F_{9/2} \rightarrow {}^4I_{15/2}$) of Er^{3+} (λ_{ex} = 980 nm) in $NaSc_{0.8}Er_{0.02}Yb_{0.18}F_4$ (UCNPs), $NaSc_{0.75}Er_{0.02}Yb_{0.18}Gd_{0.05}F_4$ (Gd:UCNPs), and $NaSc_{0.75}Er_{0.02}Yb_{0.18}Gd_{0.05}F_4$@AuNPs (Gd:UCNPs@AuNPs). The Supporting Information is available free of charge on the ACS Publications website at DOI: 10.1021/acsami.5b03218.

■ AUTHOR INFORMATION

Corresponding Author

* E-mail: sunilcfsl@gmail.com, sunilks.app@itbhu.ac.in. Tel.: +91-8574027822. Fax: +91 542 2369889.

Author Contributions

S.K.S. and M.R. contributed equally and are leading authors. A.K.S. helped in the synthesis of fluoride NPs, K.M. helped in optical measurement, and R.P. and B.K. performed biological experiments. All the authors read the manuscript.

Notes

The authors declare no competing financial interest.

■ ACKNOWLEDGMENTS

S.K.S. acknowledges the financial support from Department of Science and Technology (DST), New Delhi [DST-INSPIRE Faculty award (IFA-12 PH-21)]. M.R. is thankful to UGC, New Delhi for RFSMS junior research fellowship. A.K.S. thankfully acknowledges the DGAPA-UNAM program of postdoctoral fellowship. Thanks are also due to UGC-DAE Consortium for Scientific Research, for XRD and magnetic measurements, and AMRC, IIT Mandi, and Himanchal Pradesh for TEM and DLS measurements.

■ REFERENCES

(1) Liu, C.; Gao, Z.; Zeng, J.; Hou, Y.; Fang, F.; Li, Y.; Qiao, R.; Shen, L.; Lei, H.; Yang, W.; Gao, M. Magnetic/Upconversion Fluorescent $NaGdF_4$:Yb,Er Nanoparticle-Based Dual-Modal Molecular Probes for Imaging Tiny Tumors *in Vivo*. *ACS Nano* **2013**, *7*, 7227−7240.

(2) Singh, S. K. Red and Near Infrared Persistent Luminescence Nano-Probes for Bioimaging and Targeting Applications. *RSC Adv.* **2014**, *4*, 58674−58698.

(3) Wei, X.; Wang, W.; Chen, K. ZnO:Er,Yb,Gd Particles Designed for Magnetic-Fluorescent Imaging and Near-Infrared Light Triggered Photodynamic Therapy. *J. Phys. Chem. C* **2013**, *117*, 23716−23729.

(4) Wei, W.; Zhang, Y.; Chen, R.; Goggi, J.; Ren, N.; Huang, L.; Bhakoo, K. K.; Sun, H.; Tan, T. T. Y. Cross Relaxation Induced Pure Red Upconversion in Activator- and Sensitizer-Rich Lanthanide Nanoparticles. *Chem. Mater.* **2014**, *26* (18), 5183−5186.

(5) Shan, J.; Uddi, M.; Yao, N.; Ju, Y. Anomalous Raman Scattering of Colloidal Yb^{3+}, Er^{3+} Codoped $NaYF_4$ Nanophosphors and Dynamic Probing of the Upconversion Luminescence. *Adv. Funct. Mater.* **2010**, *20*, 3530−3537.

(6) Schäfer, H.; Ptacek, P.; Kömpe, K.; Haase, M. Lanthanide-Doped $NaYF_4$ Nanocrystals in Aqueous Solution Displaying Strong Up-Conversion Emission. *Chem. Mater.* **2007**, *19* (6), 1396−1400.

(7) Zou, W.; Visser, C.; Maduro, J. A.; Pshenichnikov, M. S.; Hummelen, J. C. Broadband Dye-Sensitized Upconversion of Near-Infrared Light. *Nat. Photonics* **2012**, *6*, 560−564.

(8) Gu, Z.; Yan, L.; Tian, G.; Li, S.; Chai, Z.; Zhao, Y. Recent Advances in Design and Fabrication of Upconversion Nanoparticles and Their Safe Theranostic Applications. *Adv. Mater.* **2013**, *25*, 3758−3779.

(9) Zhang, Y.; Liu, X. Shining a Light on Upconversion. *Nat. Nanotechnol.* **2013**, *8*, 702−703.

(10) Zhou, L.; He, B.; Huang, J.; Cheng, Z.; Xu, X.; Wei, C. Multihydroxy Dendritic Upconversion Nanoparticles with Enhanced Water Dispersibility and Surface Functionality for Bioimaging. *ACS Appl. Mater. Interfaces* **2014**, *6*, 7719−7727.

(11) Fedorov, P. P.; Luginina, A. A.; Kuznetsov, S. V.; Osiko, V. V. Nanofluorides. *J. Fluorine Chem.* **2011**, *132*, 1012−1039.

(12) Weissleder, R. A Clear Vision for In Vivo Imaging. *Nat. Biotechnol.* **2001**, *19*, 316−317.

DOI: 10.1021/acsami.5b03218
ACS Appl. Mater. Interfaces 2015, 7, 15339−15350

(13) Shi, F.; Wang, J.; Zhai, X.; Zhao, D.; Qin, W. Facile Synthesis of β-$NaLuF_4$: Yb/Tm Hexagonal Nanoplates with Intense Ultraviolet Upconversion Luminescence. *CrystEngComm* **2011**, *13*, 3782−3787.
(14) Wong, H. T.; Tsang, M. K.; Chan, C. F.; Wong, K. L.; Fei, B.; Hao, J. *In Vitro* Cell Imaging using Multifunctional Small Sized $KGdF_4$:Yb^{3+}, Er^{3+} Upconverting Nanoparticles Synthesized by a One-Pot Solvothermal Process. *Nanoscale* **2013**, *5*, 3465−3473.
(15) Khiari, S.; Bendjedaa, F.; Diaf, M. Optical Characterization of Erbium Doped KY_3F_{10} Fluoride Single Crystals. *Opt. Photonics J.* **2013**, *3*, 13−17.
(16) Sarkar, S.; Meesaragandla, B.; Hazra, C.; Mahalingam, V. Sub-5 nm Ln^{3+}-doped $BaLuF_5$ Nanocrystals: A Platform to Realize Upconversion via Interparticle Energy Transfer (IPET). *Adv. Mater.* **2013**, *25*, 856−860.
(17) Teng, X.; Zhu, Y.; Wei, W.; Wang, S.; Huang, J.; Naccache, R.; Hu, W.; Tok, A. I. Y.; Han, Y.; Zhang, Q.; Fan, Q.; Huang, W.; Capobianco, J. A.; Huang, L. Lanthanide-Doped Na_xScF_{3+x} Nanocrystals: Crystal Structure Evolution and Multicolor Tuning. *J. Am. Chem. Soc.* **2012**, *134*, 8340−8343.
(18) Mironov, V. S. Generalized Superexchange Theory of Fast Energy Transfer, Cooperative Luminescence, and Magnetic Exchange Interactions in Exchange-Coupled Pairs of Lanthanide Ions. *Spectrochim. Acta, Part A* **1998**, *54*, 1607−1614.
(19) Mironov, V. S.; Kaminskii, A. A. Covalent Mechanism of Cooperative Optical Transitions and Energy Transfer in Systems with Paired Lanthanide Ions. *J. Exp. Theor. Phys.* **1996**, *82* (5), 929−938.
(20) Das, S. G. Electronic Structure and Magnetic Properties of Scandium. *Phys. Rev. B* **1976**, *13*, 3978−3983.
(21) Yang, C. T.; Chuang, K. H. Gd(III) Chelates for MRI Contrast Agents: from High Relaxivity to "Smart", from Blood Pool to Blood−Brain Barrier Permeable. *MedChemComm* **2012**, *3*, 552−565.
(22) Leung, A. H.; Jin, J.; Wang, S.; Lei, H.; Wong, W. T. Inflammation Targeted Gd^{3+}-Based MRI Contrast Agents Imaging Tumor and Rheumatoid Arthritis Models. *Bioconjugate Chem.* **2014**, *25* (6), 1112−1123.
(23) Spedding, F. H.; Croat, J. J. Magnetic Properties of High Purity Scandium and the Effect of Impurities on these Properties. *J. Chem. Phys.* **1973**, *58*, 5514−5526.
(24) Damasco, J. A.; Chen, G.; Shao, W.; Ågren, H.; Huang, H.; Song, W.; Lovell, J. F.; Prasad, P. N. Size-Tunable and Monodisperse Tm^{3+}/Gd^{3+}-Doped Hexagonal $NaYbF_4$ Nanoparticles with Engineered Efficient Near Infrared-to-Near Infrared Upconversion for *In Vivo* Imaging. *ACS Appl. Mater. Interfaces* **2014**, *6*, 13884−13893.
(25) Wang, F.; Han, Y.; Lim, C. S.; Lu, Y.; Wang, J.; Xu, J.; Chen, H.; Zhang, C.; Hong, M.; Liu, X. Simultaneous Phase and Size Control of Upconversion Nanocrystals through Lanthanide Doping. *Nature* **2010**, *463*, 1061−1065.
(26) Bednarkiewicz, A.; Nyk, M.; Samoc, M.; Strek, W. Upconversion FRET from Er^{3+}/Yb^{3+}:$NaYF_4$ Nanophosphor to CdSe Quantum Dots. *J. Phys. Chem. C* **2010**, *114*, 17535−17541.
(27) Wang, L.; Yan, R.; Huo, Z.; Wang, L.; Zeng, J.; Bao, J.; Wang, X.; Peng, Q.; Li, Y. Fluorescence Resonant Energy Transfer Biosensor Based on Upconversion-Luminescent Nanoparticles. *Angew. Chem., Int. Ed.* **2005**, *44*, 6054−6057.
(28) He, E.; Zheng, H.; Gao, W.; Tu, Y.; Lu, Y.; Tian, H.; Li, G. Enhancement and Regulation of Fluorescence Emission from $NaYF_4$:Yb^{3+}, Er^{3+} Nanocrystals by Codoping Mn^{2+} Ions. *J. Nanosci. Nanotechnol.* **2014**, *14* (6), 4139−4146.
(29) Pang, M.; Zhai, X.; Feng, J.; Song, S.; Deng, R.; Wang, Z.; Yao, S.; Ge, X.; Zhang, H. One-Step Synthesis of Water-Soluble Hexagonal $NaScF_4$:Yb/Er Nanocrystals with Intense Red Emission. *Dalton Trans.* **2014**, *43*, 10202−10207.
(30) Greybush, N. J.; Saboktakin, M.; Ye, X.; Della Giovampaola, C.; Oh, S. J.; Berry, N. E.; Engheta, N.; Murray, C. B.; Kagan, C. R. Plasmon-Enhanced Upconversion Luminescence in Single Nanophosphor Nanorod Heterodimers Formed through Template-Assisted Self-Assembly. *ACS Nano* **2014**, *8* (9), 9482−9491.
(31) Sapsford, K. E.; Berti, L.; Medintz, I. L. Materials for Fluorescence Resonance Energy Transfer Analysis: Beyond Traditional Donor-Acceptor Combinations. *Angew. Chem., Int. Ed.* **2006**, *45*, 4562−4589.
(32) Bogdan, N.; Vetrone, F.; Ozin, G. A.; Capobianco, J. A. Synthesis of Ligand-Free Colloidally Stable Water Dispersible Brightly Luminescent Lanthanide-Doped Upconverting Nanoparticles. *Nano Lett.* **2011**, *11*, 835−840.
(33) Liu, B.; Tan, H.; Chen, Y. Upconversion Nanoparticle-Based Fluorescence Resonance Energy Transfer Assay for Cr (III) Ions in Urine. *Anal. Chim. Acta* **2013**, *761*, 178−185.
(34) Frens, G. Controlled Nucleation for Regulation of Particle-Size in Monodisperse Gold Suspensions. *Nature, Phys. Sci.* **1973**, *241*, 20−22.
(35) Munro, C. H.; Smith, W. E.; Garner, M.; Clarkson, J.; White, P. C. Characterization of the Surface of a Citrate-Reduced Colloid Optimized for Use as a Substrate for Surface-Enhanced Resonance Raman Scattering. *Langmuir* **1995**, *11*, 3712−3720.
(36) Mosmann, T. Rapid Colorimetric Assay for Cellular Growth and Survival: Application to Proliferation and Cytotoxicity Assays. *J. Immunol. Methods* **1983**, *65*, 55−63.
(37) Xia, T.; Hamilton, R. F., Jr.; Bonner, J. C.; Crandall, E. D.; Elder, A.; Fazlollahi, F.; Girtsman, T. A.; Kim, K.; Mitra, S.; Ntim, S. A.; Orr, G.; Tagmount, M.; Taylor, A. J.; Telesca, D.; Tolic, A.; Vulpe, C. D.; Walker, A. J.; Wang, X.; Witzmann, F. A.; Wu, N.; Xie, Y.; Zink, J. I.; Nel, A.; Holian, A. Inter laboratory Evaluation of *in Vitro* Cytotoxicity and Inflammatory Responses to Engineered Nanomaterials: The NIEHS Nano GO Consortium. *Environ. Health Perspect.* **2013**, *121* (6), 683−690.
(38) Ai, Y.; Tu, D.; Zheng, W.; Liu, Y.; Kong, J.; Hu, P.; Chen, Z.; Huang, M.; Chen, X. Lanthanide-Doped $NaScF_4$ Nanoprobes: Crystal Structure, Optical Spectroscopy and Biodetection. *Nanoscale* **2013**, *5*, 6430−6438.
(39) Niu, X.; Chen, H.; Wang, Y.; Wang, W.; Sun, X.; Chen, L. Upconversion Fluorescence-SERS Dual-Mode Tags for Cellular and in Vivo Imaging. *ACS Appl. Mater. Interfaces* **2014**, *6*, 5152−5160.
(40) Mohamed, M. B.; Volkov, V.; Link, S.; El-Sayed, M. A. The 'Lightning' Gold Nanorods: Fluorescence Enhancement of Over a Million Compared to the Gold Metal. *Chem. Phys. Lett.* **2000**, *317*, 517−523.
(41) Wang, Y.; Wen, T.; Zhang, H.; Sun, J.; Zhang, M.; Guo, Y.; Luo, W.; Xia, M.; Wang, Y.; Yang, B. Low-Temperature Fluorination Route to Lanthanide-Doped Monoclinic ScOF Host Material for Tunable and Nearly Single Band Up-Conversion Luminescence. *J. Phys. Chem. C* **2014**, *118*, 10314−10320.
(42) He, X.; Yan, B. One-Stone−Two-Birds" Modulation for Na_3ScF_6-Based Novel Nanocrystals: Simultaneous Morphology Evolution and Luminescence Tuning. *Cryst. Growth Des.* **2014**, *14*, 3257−3263.
(43) Ma, W. Y.; Yang, H.; Hilton, J. P.; Lin, Q.; Liu, J. Y.; Huang, L. X.; Yao, J. A Numerical Investigation of the Effect of Vertex Geometry on Localized Surface Plasmon Resonance of Nanostructures. *Opt. Express* **2010**, *18*, 843−853.
(44) El-Brolossy, T. A.; Abdallah, T.; Mohamed, M. B.; Abdallah, S.; Easawi, K.; Negm, S.; Talaat, H. Shape and Size Dependence of the Surface Plasmon Resonance of Gold Nanoparticles Studied by Photoacoustic Technique. *Eur. Phys. J.: Spec. Top.* **2008**, *153*, 361−364.
(45) Yang, H. H.; Zhang, S. Q.; Chen, X. L.; Zhuang, Z. X.; Xu, J. G.; Wang, X. R. Magnetite-Containing Spherical Silica Nanoparticles for Biocatalysis and Bioseparations. *Anal. Chem.* **2004**, *76*, 1316−1321.
(46) Singh, S. K.; Kumar, K.; Srivastava, M. K.; Rai, D. K.; Rai, S. B. Magnetic-Field-Induced Optical Bistability in Multifunctional Gd_2O_3:Er^{3+}/Yb^{3+} Upconversion Nanophosphor. *Opt. Lett.* **2010**, *35* (10), 1575−1577.
(47) Ahmad, S.; Nagarajan, R.; Raj, P.; Prakash, G. V. Novel Fluorite Structured Superparamagnetic $RbGdF_4$ Nanocrystals as Versatile Upconversion Host. *Inorg. Chem.* **2014**, *53*, 10257−10265.
(48) Priyam, A.; Idris, N. M.; Zhang, Y. Gold Nanoshell Coated $NaYF_4$ Nanoparticles for Simultaneously Enhanced Upconversion Fluorescence and Darkfield Imaging. *J. Mater. Chem.* **2012**, *22*, 960−965.

DOI: 10.1021/acsami.5b03218
ACS Appl. Mater. Interfaces 2015, 7, 15339−15350

(49) Yuan, P.; Lee, Y. H.; Gnanasammandhan, M. K.; Guan, Z.; Zhang, Y.; Xu, Q. H. Plasmon Enhanced Upconversion Luminescence of $NaYF_4$:Yb,Er@SiO_2@Ag Core−Shell Nanocomposites for Cell Imaging. *Nanoscale* **2012**, *4*, 5132−5137.
(50) Kannan, P.; Rahim, F. A.; Chen, R.; Teng, X.; Huang, L.; Sun, H.; Kim, D. H. Au Nanorod Decoration on $NaYF_4$:Yb/Tm Nanoparticles for Enhanced Emission and Wavelength-Dependent Biomolecular Sensing. *ACS Appl. Mater. Interfaces* **2013**, *5* (9), 3508−3513.

DOI: 10.1021/acsami.5b03218
ACS Appl. Mater. Interfaces 2015, 7, 15339−15350